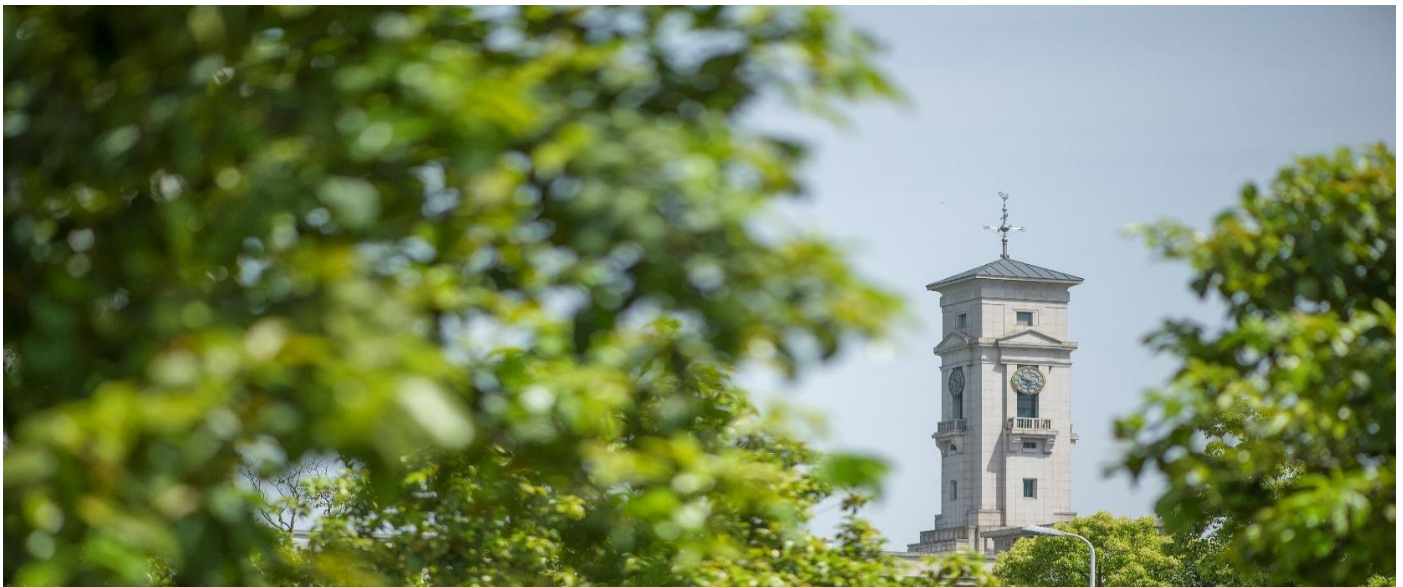


# Electrode-molecule energy level offsets in a gold-benzene diamine-gold single molecule tunnel junction

Mark S. Szepieniec, James C. Greer



**University of  
Nottingham**

UK | CHINA | MALAYSIA

University of Nottingham Ningbo China, 199 Taikang East Road, Ningbo, 315100, Zhejiang, China.

First published 2020

This work is made available under the terms of the Creative Commons Attribution 4.0 International License:

<http://creativecommons.org/licenses/by/4.0>

The work is licenced to the University of Nottingham Ningbo China under the Global University Publication Licence:

<https://www.nottingham.edu.cn/en/library/documents/research/global-university-publications-licence-2.0.pdf>



**University of  
Nottingham**

UK | CHINA | MALAYSIA

# Electrode-molecule energy level offsets in a gold-benzene diamine-gold single molecule tunnel junction

Mark S. Szepieniec<sup>1</sup> and James C. Greer<sup>2,\*</sup>

<sup>1</sup>*Tyndall National Institute, University College Cork,  
Lee Maltings, Dyke Parade, Cork, T12 R5CP, Ireland*

<sup>2</sup>*Department of Electrical and Electronic Engineering,  
Nottingham Ningbo New Materials Institute,  
University of Nottingham Ningbo China,  
199 Taikang East Road, Ningbo, 315100, China*

(Dated: September 28, 2020)

## Abstract

One means for describing electron transport across single molecule tunnel junctions (MTJs) is to use density functional theory (DFT) in conjunction with a nonequilibrium Green's function (NEGF) formalism. This description relies on interpreting solutions to the Kohn-Sham (KS) equations used to solve the DFT problem as quasiparticle (QP) states. Many practical DFT implementations suffer from electron self-interaction errors and an inability to treat charge image potentials for molecules near metal surfaces. For MTJs, the overall effect of these errors is typically manifested as an overestimation of electronic currents. Correcting KS energies for self-interaction and image potential errors results in MTJ current-voltage characteristics in close agreement with measured currents. An alternative transport approach foregoes a QP picture and solves for a many-electron wavefunction on the MTJ subject to open system boundary conditions. It is demonstrated that this many-electron method provides similar results to the corrected QP picture for electronic current. Analysis of these two distinct approaches are related through corrections to a junction's electronic structure beyond the KS energies for the case of a benzene diamine molecule bonded between two gold electrodes.

---

\*jim.greer@nottingham.edu.cn

## I. INTRODUCTION

Determining the conductance for single molecule tunnel junctions (MTJs) has been a subject of experimental and theoretical investigation for over two decades [1, 2]. To reconcile theoretical predictions with experimental observations for the conductance across a MTJ is often challenging due to the difficulties in predicting or measuring energy level spacings and offsets for occupied and unoccupied states in a MTJ, as well as the difficulties in determining the geometries for molecules bonded between two metallic electrodes. Combining theoretical and experimental efforts has nonetheless led to greater understanding for charge transport mechanisms in MTJs.

Theoretical calculations for electronic currents often require empirical corrections or highly accurate electronic structure computations, or in instances both approaches are required in tandem. From a simplified viewpoint, a molecule in a MTJ may be thought of as a tunnelling barrier with the magnitude of the potential barrier given by the energy difference between the quasi-Fermi levels in the electrodes and the highest or lowest occupied molecular orbital (HOMO/LUMO) energy levels. At low applied voltages and assuming non-resonant tunnelling, a potential barrier model provides a reasonable estimate of tunnelling currents. In this picture, the barrier height and width are the key physical quantities for predicting charge transport. Of course, the barrier model as described is an oversimplification of the true electronic structure of a MTJ. More accurate electronic structure descriptions include effects due to charge transfer and geometry variations accompanying the bonding of a molecule between electrodes. To describe these effects, the treatment of hybridization between molecular and electrode electronic states is required.

To provide a description of the energy levels within a MTJ to predict transport properties, a common strategy is to combine the non-equilibrium Green's functions (NEGF) [3–5] formalism together with density functional theory (DFT) [6], an approach sometimes designated NEGF+DFT [7]. Significant understanding has been achieved in relating measured current-voltage (IV) characteristics to the electronic structure of MTJs within this framework. There remain however shortcomings in obtaining quantitative agreement to reconcile experiment within this approach that typically lead to a systematic over-estimation of electronic current. This deficiency is primarily attributed to two causes. The first of these is the well-documented band gap underestimation if using Kohn-Sham orbital energies as

quasiparticle (QP) energies obtained from typical approximations to the DFT exchange-correlation (XC) functional [8]. The ‘band gap problem’ results from spurious electron self-interactions errors [9] that are not explicitly cancelled or compensated for within many XC approximations. In terms of a simple barrier model, the band gap problem manifests as an underestimation of the potential barrier and hence an over-estimation of tunnelling transmission. A second difficulty facing many approximate DFT approaches in describing a MTJ is a poor description of image charge potentials for molecules absorbed at or bonded to metal surfaces [10]. An approach to overcome these shortcomings is to add self-energy corrections to the Kohn-Sham energy levels that compensate electron self-interactions and then to add corrections that also describe the image charge potential. This and related approaches have been shown to yield results in quantitative agreement with experiments [11–16]. Corrections for the electron self-interaction typically rely on computationally demanding *GW* calculations. Suggestions for alternative approaches using less demanding computations of the self-interaction correction and classical electrostatics have been demonstrated to improve the description of the image potential relative to uncorrected NEGF+DFT [10, 11, 15, 16].

The methods described up to this point retain a QP description of the junction electronic structure. Alternative approaches focusing on calculation of the electronic current from a direct determination of a density matrix (DM) forego a QP picture [17–23]. These methods apply different methods but they share in common that non-equilibrium boundary conditions appropriate to electronic transport [24] are imposed directly to the calculation of DMs. In contrast to NEGF+DFT methods based on the Kohn-Sham equations, direct calculation of a DM or determining a one electron reduced DM (1e-RDM) from a many-electron wavefunction does not need to invoke the use of QP energies. Hence relating electronic currents calculated from a determination of a DM or a RDM to the potential barrier model is not immediate.

Herein many-electron correlated scattering (MECS) [17–19] is applied which relies on a many-electron wavefunction method, configuration interaction (CI), to calculate a 1e-RDM subject to open system boundary conditions. Previously, MECS has been applied to single MTJs consisting of benzene dithiol [17, 18], alkane dithiol [25], alkane diamine [26], silane dithiol/diamine [27], and point contacts [28]. These calculations demonstrate that MECS predicts electronic currents consistent with measured molecular conductance. The agreement with experiment suggests that deficiencies associated with the NEGF+DFT approach do

not arise or are less severe when using a many-electron wavefunction treatment of a MTJ's electronic structure. To explore if improved molecular conductance predicted from MECS calculations can be directly related to the improvements resulting from correcting the QP energy spectrum by self-interaction and image potential correction is the subject of this study. The experimentally well-characterized BDA MTJ has been chosen as the test case to compare between the two distinct approaches to electronic charge transport.

## II. METHODS

Previously, Quek *et al.* showed with correction terms to QP energies that theoretical predictions can be made in agreement with low voltage conductance statistics measured from a series of traces for a gold break junction in a BDA molecular solution [11]. A gold electrode-BDA-gold electrode model based upon DFT calculations is also described by the authors. Their NEGF+DFT model is used as a reference point for calculation of IV characteristics which they subsequently used correction terms to improve. Based on various tip geometries built from semi-infinite electrodes with a bonding tip on an otherwise planar Au (111) surface or from pyramidal point contact models, it is found for molecules with amine linkers bonding to Au electrodes that IV characteristics are not sensitive to the exact bonding geometry of the linker to the electrode ‘tip’ [11, 26]. To ensure that a common starting point between the previous calculations and this work, a key consideration in addition to the junction's explicit atomic structure is that similar electronic structure treatments for the uncorrected NEGF+DFT calculations are used in this study to enable a comparison to the previous calculations reported in ref. [11].

FIG. 1: Explicit atomic model of the MTJ: a single benzene diamine molecule linked by amine groups to two pyramidal gold clusters. Yellow: Gold, Green: Carbon, Blue: Nitrogen, and White: Hydrogen. The junction axis is taken to run between the two gold electrode tips in the diagram.

The DFT calculations undertaken by Quek *et al.* are obtained using localized atomic orbitals and periodic boundary conditions for treating the electrodes. Their basis makes use of numerical split valence polarized atomic orbitals (PAO), details of which are available in their supplementary material [11]. As the goal in this work is to apply a CI calculation

to determine the 1e-RDM, it is advantageous to use a DFT program that does not apply periodic boundary conditions motivating the choice of the Turbomole quantum chemistry programs [29, 30] for the DFT calculations. Turbomole applies Gaussian atomic basis sets and a double zeta basis including polarization is selected for the molecular atoms (C, N, H). However, care is taken in selecting basis sets to produce results comparable to those of Quek *et al.* This is accomplished by comparing the Kohn-Sham orbital energies from DFT calculations on isolated atoms and for the molecular orbitals of BDA. To describe Au atoms for the electrode model, a basis with 11 explicit electrons is applied by Quek *et al.* In contrast to their approach, CI calculations are required in the following as a first step to obtain corrections beyond the NEGF+DFT model. Explicit electrodes must also be included in the CI calculations and this is done using pyramidal electrodes with a tip geometry similar to that used in ref. [11]. Similar electrode structures have been studied in detail for the calculation of the conductance quantum in point contacts using the MECS approach [28]. For MECS calculations, a CI expansion is used to determine a many-electron wavefunction. The length of a CI expansion increases combinatorially with the number of electrons and single electron basis functions. Treating electrodes with a large number of electrons or basis functions becomes impractical due to the resulting rapid increase in the length of the CI expansion. To limit the number of explicit electrons, the electrode Au atoms are split into two groups. The four atoms closest to the molecule at each electrode (one Au apex atom and three Au atoms in the second layer of the electrode tip) are treated with an 11-electron basis set. For the remaining Au atoms, a basis with only one explicit electron and four basis functions, representing each Au atom's 6s orbital, with the addition of three diffuse p-type functions, are used. The limitations of the finite cluster approximation and extending the electrodes is considered in detail in ref. [28]. Using the same bond lengths and bond angles for the electrode tip and linker molecules as reported by Quek *et al.*, the gold-BDA-gold MTJ is constructed and taken as a starting geometry. The structure is then allowed to relax (minimization of energy with respect to atomic positions) using the Perdew-Burke-Ernzerhof (PBE) XC functional which implements a generalized gradient approximation (GGA) for the charge density. The atomic positions are relaxed using the same force threshold as used in ref. [11] The final junction geometry is shown in fig. 1.

For the NEGF+DFT calculations, electrode self-energies are computed from repeat units consisting of the two back planes of the explicit electrode. It is found that six layers of

Au atoms (3 repeat units) form an electrode cell that is sufficiently large to make next-nearest-neighbour interactions between cells negligible. This model of the junction and semi-infinite electrodes are then used with the TiMeS quantum transport program [31] to calculate electron transmission. The TiMeS program uses semi-analytical expressions for the Green's functions in the NEGF formalism for which the limit for the artificial broadening parameter approaching zero has been taken. This is in contrast to most transport programs that rely on numerical determination of the Green's function resulting in a broadening and smoothing of resonance peaks. To determine electron transmission within the NEGF+DFT approach, the relevant Fock matrices, interaction matrices, and orbital overlaps are extracted from the Kohn-Sham calculations to build a device Hamiltonian and electrode self-energies in a localized atomic orbital basis to allow partitioning into a device region, left electrode, and right electrode.

After establishing a QP basis that can reasonably reproduce the junction transmission at the NEGF+DFT level, a CI calculation is then used to improve the electronic structure description of the junction. The Kohn-Sham orbitals are then used to build spin-projected Slater determinants or configuration state functions (CSFs) which are used to form the CI expansion [32–34]. To provide an accurate picture of the electronic current in the MECS formalism, it is necessary to include several excited states to allow coupling to the ground state as a voltage is applied. The voltage generates an electric field between the electrodes that couples excited states to the ground state resulting in polarization of the junction. The coupling can be explained by the fact that the energy change caused by an applied electric field is proportional to dipole interaction matrix elements of the applied electric field. To lowest order, the coupling to ground state is

$$\Delta E = e^2 \mathcal{E}^2 \sum_{i \neq 0} \frac{|\langle \Psi_0 | \hat{x} | \Psi_i \rangle|^2}{E_i - E_0}. \quad (1)$$

Here,  $\mathcal{E}$  is the magnitude of the electric field, the summation runs over all excited many-body states, and the direction of the field is taken along the transport axis selected to be the  $x$ -direction. The electric field operator is anti-symmetric with respect to inversion symmetry in the junction. Excited states with the same symmetry with respect to inversion as the ground state will not couple in the summation for the polarizability energy. For the case of the junction studied in this work, which has  $C_{2h}$  symmetry, there are four irreducible representations (irreps) denoted  $a_1$ ,  $a_2$ ,  $b_1$ , and  $b_2$ . Application of the electric field breaks

symmetry along the transport direction,  $a_1$  states therefore couple to  $b_2$  states, and likewise  $a_2$  states will couple to  $b_1$  states. The many-electron ground state has  $A_1$  symmetry. As the junction polarizes, the current-carrying state to lowest order can be described as a superposition of non-polarized  $A_1$  and  $B_2$  states. Excited states of opposing parity under inversion to the ground state increasingly couple with increasing electric field strength, and therefore become increasingly important in the CI expansion as a voltage is applied across the MTJ.

The previous observations suggest a procedure for pre-selecting important CSFs to describe the junction as a voltage is applied. To accurately capture the polarization of the junction and likewise the current induced by the open system boundary conditions, a set of CSFs to be included in the MECS calculation can be found from the lowest excited CSFs that couple to the unperturbed (zero voltage) wavefunction through the dipole matrix elements. Following this reasoning, the many-electron transport basis is performed using a Monte Carlo Configuration Interaction (MCCI) calculation with a CI coefficient threshold  $c_{\min} = 0.01$  [35, 36]. To generate the excited CSFs of opposing parity, an electron from the highest occupied  $a_1$  molecular orbital (MO) is transferred to the lowest unoccupied  $b_2$  MOs. The three lowest energy  $B_2$  CSFs provide approximations to the first three  $B_2$  excited states. Additionally, singly excited CSFs of  $A_1$  symmetry are included in the CI expansion as Kohn-Sham orbitals are used so that Brillouin’s theorem does not exclude the single excitations. The role of the  $A_1$  single excitations may be understood from Thouless’ theorem [37] which relates two non-orthogonal Slater determinants  $|\Psi\rangle$  occupied with  $N$  electrons selected from  $M$  spin orbitals by

$$|\Psi'\rangle = \mathcal{N} \exp\left(\sum_{i=N+1}^M \sum_{j=1}^N c_{ij} a_i^\dagger a_j\right) |\Psi\rangle, \quad (2)$$

which can for small coefficients  $c_{ij}$  be approximated as

$$|\Psi'\rangle \approx \mathcal{N} \left(1 + \sum_{i=N+1}^M \sum_{j=1}^N c_{ij} a_i^\dagger a_j\right) |\Psi\rangle, \quad (3)$$

where  $a_i^\dagger, a_j$  are creation and annihilation operators, respectively,  $|\Psi\rangle, |\Psi'\rangle$  represents Slater determinants, and  $\mathcal{N}$  is the normalization. Hence for weak electric fields across the MTJ, the effect of including the  $A_1$  singles allows a ‘re-optimization’ of the the reference state, as well the  $A_1$  single excitations couple to the excited  $B_2$  states as the electric field is introduced. This procedure results in a CI vector including only 1890 CSFs. The resulting CI expansion

provides a compact description of electron-electron correlations and polarizability of the MTJ.

The MECS method relies on the use of the Wigner phase-space distribution function [38, 39] to constrain the 1e-RDM to open boundary conditions [17–19]. Constraints are applied to ensure the momentum flowing from the electrodes into the molecule remain unchanged as a voltage is applied - consistent with the condition that the electrodes are locally in equilibrium. To the contrary, electrons entering the left and right electrodes from the molecular region do not fulfil detailed balance as voltage difference is applied across the junction resulting in a net electronic current flow. It is assumed the electrons scattered into the electrodes rapidly re-equilibrate to ensure the electrodes remain locally in equilibrium.

To apply the boundary conditions for the electrodes, the Wigner function  $f(q, p)$  is calculated from the 1e-RDM obtained from the CI wavefunction allowing for a semiclassical picture of the momentum  $p$  at a given position  $q$  to be described by the quasi-probability distribution function  $f$ . Due the uncertainty principle, the Wigner phase-space distribution is not a true probability distribution function as it is not everywhere positive nor is it a unique phase space representation for quantum mechanics [24, 38, 39]. Nonetheless, in many cases the Wigner function is known to provide a semi-classical picture for electron distributions and this has been previously demonstrated for semiconductor devices and for the metal electrodes used in break junction experiments [28]. For MECS calculations, a plane normal to the current flow in each electrode is chosen and the Wigner function is averaged over this plane to give a one-dimensional representation of the momentum flowing across the plane. At zero voltage bias, the distributions in each electrode are symmetric indicating that the net momentum flow in and out of the MTJ balances to zero at each electrode, there is no current. As an electric field is applied across the molecular region, the electrode equilibrium condition requires the inward flow to remain the same as at zero voltage. However the potential difference across the MTJ gives rise to asymmetric scattering between left and right incoming electrons. MECS calculations apply a constrained energy minimization procedure to fix the momentum flow from the electrodes to their equilibrium (zero applied voltage) value as an electric field is applied. The momentum flow out of the molecular region into either electrode is unconstrained. The method of Lagrangian multipliers is applied to constrain the Wigner function, and additional Lagrangian multipliers are used to force the current magnitude to be constant between points at which current constraints are applied.

The latter constraints are introduced to mitigate the violation of current continuity due to the variational nature of the calculation and finite basis effects.

In order for the assumption that the incoming electron momentum distributions at the Wigner planes remain in equilibrium with the fictional electron reservoirs, the Wigner planes need to be positioned within the finite electrode model at a position that minimizes edge effects [28]. Consideration of the placement of the Wigner planes focuses on the region in the electrodes between 7.5 and 9.5 a.u. ( $\sim 0.4$  nm to  $\sim 0.5$  nm) as measured relative to the apex atom of the electrode tip. Within this central region in the electrodes, the Wigner distribution is relatively stable against displacements of the constraint planes. This stability is attributed to the rapid decay with distance of the 1e-RDM within a metal thus minimizing finite size effects. Five values for the position of the Wigner constraint plane are considered: 7.5, 8.0, 8.5, 9.0, and 9.5 a.u. again referenced to the electrode tip. By constraining the Wigner function, the momentum flow from the electrodes into the molecule region  $pf_L(q, p > 0)$  and  $pf_R(q, p < 0)$ , where  $L, R$  denote the left and right electrodes, respectively, enforces the equilibrium condition on the electrodes. For low values of the Wigner momentum, the product  $pf(q, p)$  is negligible, and at larger values of momenta the Wigner function becomes negligible. Hence enforcing the boundary conditions at intermediate values of momenta has the most effect on electronic currents [28].

The CI variational problem is typically solved through the associated matrix eigenvalue problem. However in the MECS formulation additional constraints as those arising from imposition of the scattering boundary conditions [24] and current continuity as are required. The associated eigenvalue becomes non-linear due to the constraint conditions and standard methods for solving the CI problem are not applicable. Treating the variational problem as a constrained minimization problem allows for the determination of a many-body wavefunction satisfying open system boundary conditions for the current-carrying state induced by the applied electric field  $\mathcal{E}$ . The Lagrange multiplier penalty method function is applied to the minimization problem by defining the augmented Lagrangian  $\mathcal{L}$  by

$$\mathcal{L}(\Psi, \lambda_i, \sigma) = \langle \Psi | (\hat{H} + \mathcal{E}z) | \Psi \rangle - \sum_i \lambda_i c_i(\Psi) + \frac{1}{2} \sigma \sum_i c_i^2(\Psi), \quad (4)$$

where  $z$  is chosen as the transport axis. The first term is the unconstrained many-electron energy for the junction with application of an external electric field represented as a CI expansion, the second term is the sum of Wigner function and current continuity constraint

violations with their respective Lagrangian multipliers  $\lambda_i$ , and the third term is a penalty term introduced to aid in the numerical convergence and stability of the minimization procedure. Further details can be found in refs. [17–19].

The steps involved in the MECS approach may be summarized as:

1. solve the CI problem for the explicit molecular junction in the absence of an external electric field (zero voltage bias)
2. from the many electron wavefunction, calculate the 1e-RDM
3. transform the 1e-RDM to obtain the Wigner distribution function  $f_0(\vec{q}, \vec{p})$  at zero voltage
4. integrate the zero voltage Wigner distribution function on a planes normal to the transport direction in the left and right electrodes to obtain a one dimensional representation of the Wigner function  $f_0(q, p)$  (i.e. integrate the Wigner momentum in flow and out flow across a plane in the electrode)
5. in the left electrode select values  $f_0(q_L, p > 0)$  and in the right electrode select values  $f_0(q_R, p < 0)$  to constrain the momentum flow into the molecular region to the equilibrium value (reservoir boundary conditions),  $q_L$  and  $q_R$  denote the position of the Wigner constraint planes in the left and right electrodes, respectively
6. introduce a voltage across the scattering region by application of an external electric field  $\mathcal{E}$
7. minimize the Lagrangian function and calculate the resulting 1e-RDM resulting from the application of the external electric field
8. calculate the current from the 1e-RDM; see eq. 5
9. repeat the procedure from step 6 at each voltage bias required

The choice of the Wigner function to impose open system boundary conditions is a convenient choice [24]. However, the MECS method is not restricted to use of the Wigner function, any distribution that defines the momentum flowing into and out of each electrode can be used to constrain the 1e-RDM. Also, the integration of the Wigner momentum across

a plane in the electrodes is also not strictly required, constraints at several points across the plane in the electrodes can be used. However, for computational efficiency it is found that constraining the total momentum crossing the plane for the Wigner momenta  $p$  is sufficient to treat the electrodes as electron reservoirs in equilibrium.

The current-voltage measurements reported in ref. [11] are limited to the linear regime with a maximum applied voltage of 25 mV. The MECS transport calculations are therefore also limited to the low bias regime. Obtaining converged currents at low voltages requires careful selection of several tolerances required by the VICI program which implements the MECS formalism [18]. The key parameters to ensure convergence are checked after each iteration of the minimization procedure at a given voltage and are chosen as: change in objective function  $< 3 \times 10^{-7}$ , change in the objective functions gradient magnitude  $< 10^{-5}$ , and constraint violation tolerance  $< 3.16 \times 10^{-6}$ . Once convergence with respect to these parameters has been verified, there are two remaining parameter sets to determine: the position of the Wigner planes and the number of planes to apply current continuity. These parameters are further explored in the following section.

### III. RESULTS AND COMPARISON

Fig. 2 compares the electron transmission as a function of energy obtained from the NEGF+DFT calculations described for this work in the previous section to the results from Quek *et al.* The Fermi level  $E_F$  for the junction geometry is taken to be -4.7 eV corresponding to the HOMO for the entire junction. That this choice of the Fermi energy corresponds to highest occupied state in the metal electrodes is validated by a calculation of the energy levels for the isolated electrodes. Hence the junction Fermi level can be equated to the Au electrodes' work function.

FIG. 2: Comparison of transmission as a function of energy for the junction in figure 1 and compared to similar calculations from ref. [11]. Both calculations use the NEGF+DFT calculation on similar geometries using similar electronic structure approximations.

Comparing the two calculations as presented in fig. 2, agreement is found for the transmission resonances occurring for unoccupied states and reasonable agreement is found for

resonances corresponding to states near the Fermi level, with the latter determining the current-voltage characteristics at low voltage bias. A resonance transmission peak can be seen approximately 1 eV below the Fermi level, which is identified as the molecular HOMO hybridized to the metallic electrode states [11]. The transmission calculation from this work finds two narrow peaks approximately 1.0 eV below  $E_F$ . The peak slightly lower in energy is located below -1.0 eV approximately aligning to the single resonance seen by Quek *et al.*, and a sharper resonance slightly above -1.0 eV overlapping with the shoulder of the peak found by Quek *et al.* A similar double peak structure for the resonance is seen in the work of Strange *et al.* [13] who use a non-planar electrode with a single bonding apex Au atom. However in their work resonances from DFT are lower in energy relative to the Fermi level, possibly due to differences in basis sets, XC potential, and the details of the bonding geometry to the tip. The broader peaks found in the calculation of ref. [11] are due in part to their planar electrode structure relative to the pyramidal electrode model used in this work. The planar electrode model is a better approximation to the wide band limit expected to well approximate gold electrodes, whereas in this work the electrode is a nanowire structure leading to the gold tips as described in sect. II leading to a less bulk-like density of states. Also, as previously mentioned, the TiMeS program uses a semi-analytic version of the Green's functions and no artificial broadening is introduced. However, the overall hybridization of the molecular states to the tips of the gold electrodes is seen to be comparable between the two models. Additional differences likely arise from the specific bonding geometries and the atomic orbital basis set differences between the two calculations. However, the behavior and descriptions are in overall strong agreement. These NEGF+DFT results are taken as the zero<sup>th</sup> order reference between subsequent calculations that include corrections beyond the two DFT models used to generate fig. 2.

The MECS based transport calculations are next considered using the CI expansion as described in sect. II. The MECS transport calculations enables a determination of the molecular conductance which is then compared to the experimental and theoretical estimates found in ref. [11] to evaluate electronic structure corrections beyond the NEGF+DFT approximation. The electronic current density in the MECS approach is calculated directly from the 1e-RDM as

$$J(\vec{r}) = \frac{e\hbar}{2im_0} \left[ \vec{\nabla}_{\vec{r}} - \vec{\nabla}_{\vec{r}'} \right] \rho(\vec{r}, \vec{r}')|_{\vec{r}=\vec{r}'}, \quad (5)$$

where  $\rho(\vec{r}, \vec{r}')$  is the 1e-RDM,  $e$  is the electron charge,  $\hbar$  is Planck's constant divided by  $2\pi$ ,

and  $m_0$  is the electron mass. The current density is integrated over planes normal to the transport direction. The MECS method relies on minimizing the many-electron energy over the explicit MTJ subject to the application of the open-system boundary conditions [18, 24], as well as the inclusion of current constraints. The energy is an integrated quantity and the minimization procedure does not ensure that the RDM calculated from a finite CI expansions is uniformly accurate at each position. Hence the calculation of the current can vary from plane-to-plane. This motivates adding local current continuity conditions to the constrained minimization procedure. These additional constraints are imposed by requiring the current calculated on two subsequent planes normal to the transport direction to be within a specified tolerance. Fig. 3 shows the current as a function of the number of current constraint planes and for five values of the Wigner plane positions. The dashed line shows the experimental average value for junction conductance of  $0.0064 G_0$ , which corresponds at 0.025 V to a current of 12.4 nA. Note, that the experimental distribution of the conductance values display a half-width of  $47 \pm 8\%$  obtained as reported in ref. [11]. In fig. 3, the experimental value is given as a dashed line and the half-width for the corresponding current values are shown as the shaded region. In general, there is a downward trend as the number of current constraints is increased, with the downward trend notably increasing when applying a large number of constraints, or equivalently as the spacing between constraints is decreased. Another observation is that the current generally decreases as the distance between Wigner constraint planes in the left and right electrodes is decreased. This behavior is consistent with the previous observation: as the Wigner planes are placed closer together for a fixed number of current constraints, the spacing between the current constraints is decreased. In general, it is found for reasonable values for the location and spacing of the constraint conditions within the explicit junction region, the majority of MECS predicted currents are well within the measured spread for the BDA MTJ.

Several sources for errors when calculating the current from the 1e-RDM matrix can be identified. These errors relate to the variational nature of the calculation and finite basis expansions. The errors are ultimately related to the finite atomic orbital (AO) expansion of the molecular orbitals used to express the CI wavefunction and the 1e-RDM matrix. The current density calculated from the 1e-RDM matrix can be shown in a finite basis set approximation to have a maximum least squares error, and that the maximum error decreases with increasing basis set size when using orbitals that diagonalize the 1e-RDM or

FIG. 3: Currents calculated in the MECS formalism as a function of the number of planes through on which the current is constrained to be approximately equal. Five different Wigner plane positions are shown with all displaying a general trend of decreasing current as a larger numbers of current constraint planes are introduced. Decreasing current values as the Wigner planes are placed closer together thereby reducing the distance between the planes at which the current constraints are applied. The black dashed line is the experimental electronic current from ref. [11] and the shaded area illustrates the current range corresponding to the half-width of the measured conductance histogram.

natural orbitals. However, the error can be lower than this maximum and convergence need not be monotonic as the expansion is increased. As well, the error varies point-to-point [40]. A second source of error is that the molecular orbitals used to construct the CI wavefunction are calculated from a finite cluster model and are not open system (current-carrying) orbitals. The ability of the CSFs constructed from these orbitals to carry a current relies on the use of complex CI coefficients within a MECS calculation. This leads to an additional error leading to point-point variations when constructing the 1e-RDM from these orbitals. This can be understood in analogy to approximating a momentum eigenstate from particle-in-a-box (PiB) wavefunctions. For a rectangular potential well of length  $L$ , the (unnormalized) eigenfunctions defined on  $[-L/2, +L/2]$  are given by

$$\begin{aligned}\psi_n(x) &\propto \cos\left(\frac{n\pi}{L}x\right) & n \text{ odd,} \\ \psi_n(x) &\propto \sin\left(\frac{n\pi}{L}x\right) & n \text{ even.}\end{aligned}\tag{6}$$

To approximate a momentum eigenstate, the approximation  $\psi(x) = \psi_n(x) + i\psi_{n+1}(x)$  is used. Assume  $n$  is odd, the current density in this approximation is proportional to

$$J(x) \propto \frac{n\pi}{L}\cos\left(\frac{\pi}{L}x\right) - \frac{\pi}{2L}\sin\left(\frac{2n\pi}{L}x\right)\sin\left(\frac{\pi}{L}x\right)\tag{7}$$

which is at larger values of  $n$  is approximately equal to the current from a momentum eigenstate  $k_n = n\pi/L$  multiplied by a broad envelope function that is maximum at  $L = 0$ . The second term represents a low amplitude, rapid oscillation in current with an envelope function that is a minimum at  $L = 0$ . Note the difference of a factor of 2 in the wavevector

due to the finite boundary conditions for the PiB eigenstates compared to a plane wave state. However to generate a current carrying state with this approximation arises from the superposition between a pair of PiB eigenstates with  $\Delta n = 1$  effectively restoring the factor of 2. The best approximation to the current occurs in the central region on which the expansion functions are defined, near the point where the envelope for the first term reaches a maximum. Similar finite basis errors occur when calculating the current density from the 1e-RDM expressed from molecular (or natural) orbitals that are calculated without open boundary conditions (*i.e.* from a finite cluster). For a many-electron system, however, oscillations from multiple terms are combined to determine a 1e-RDM. A CI vector with sufficient variational degrees of freedom is required to compensate for the errors in the calculation of the physical current within such a scheme. However, as will be demonstrated, a reasonable approximation can be achieved from an optimised set of configurations in a short CI expansion and with the introduction of current continuity constraints.

To investigate these effects in building the 1e-RDM, the current as a function of position through the BDA MTJ is considered. The influence of the number and position of the current constraints is shown in fig. 4 with the Wigner planes for enforcing the open system boundary conditions located at 9.0 a.u. from each electrode tip, and for three different choices for the number of current constraints placed uniformly between the Wigner planes. In fig. 4a, there are five positions between which current continuity is imposed. The average current results in a reasonable approximation to the average experimental current. However, the low number of current constraints results in large violations of current continuity between the positions at which the current constraints are applied. For the intermediate value of eleven current constraints as shown in fig. 4b, the magnitude of the current reduces but is still within the experimental range, and the current continuity violations between the positions of the current constraints is significantly reduced. If the the number of current constraints is chosen larger as in fig. 4c with seventeen constraints, the larger number of constraints results in a slight reduction in violation of current continuity but also produces a significant reduction in the current through the junction.

The three examples in fig. 4 highlight the effects of the current constraints. In fig. 4a, the violation of current continuity is large but with the average current providing a reasonable approximation to measured currents. Fig. 4b provides a much improved current profile over the explicit junction region and the current magnitude remains in good agreement

FIG. 4: Current as a function of position through the BDA MTJ at an applied voltage of 0.025 V with Wigner boundary conditions applied at 9.0 a.u from each of the electrode tips with (a) five, (b) eleven, and (c) seventeen equally spaced positions at which current constraints are applied. The apex Au atoms in the electrodes are located at approximately  $\pm 8$  a.u from the origin. Horizontal red lines show the averaged current for each calculation, and vertical dashed black lines indicate the positions where the current constraints are enforced.

with experiment. Further increasing the number of current constraints as in fig. 4c does not significantly improve current continuity but results in a significant reduction in the predicted current. The calculations highlight that the 1e-RDM is expressed in molecular orbitals built from localized AOs. The most rapid oscillations in the one-electron wavefunctions allowed due the choice of this type of basis set is on the order of the interatomic spacing. Selecting the spacing of the current constraints larger or smaller relative to the atomic spacing in the MTJ as in figs. 4a and c results in under- or over-constrained solutions, respectively.

Hence the analysis leads to the conclusion that choosing the constraints to the Wigner function should be chosen at planes in the electrodes where the Wigner distribution is stable against small variations in position. For the current constraint spacings, the best choice is to choose a spacing that is of the order of the interatomic spacing within the molecular region to ensure a current that approximately satisfies current continuity but without imposing constraints that are not consistent with the use of the AO expansions. With appropriate choices for the constraint conditions guided by physical based models, predicted currents comparable to the experimental measurements are found.

The currents found apply the MECS approach are in good agreement with both the experimental work and the NEGF+DFT corrected values reported by Quek *et al.* The physically motivated corrections in their work are designed to provide a better molecular HOMO energy relative to the electrode work function to describe the potential energy barrier across the molecule. The fact that the MECS calculation obtains similar current magnitudes for a wide range of simulation parameter seems to indicate that the energy levels as corrected in ref. [11] are in some sense reproduced by the CI treatment of the molecular junction. Indeed, if it is assumed the molecule gives rise to approximately a rectangular potential

barrier, the width of which is determined by the geometry of the junction, then the fact that similar currents are obtained in both approaches implies the effective potential barriers must be of comparable energies. To determine to what level these expectations are met, a comparison of the junction energy level alignments between the two methods is considered.

The level alignment between the HOMO of the BDA molecule with respect to the metal's Fermi level within the DFT treatment of the MTJ results in an overestimation by approximately a factor of seven relative to the measured current before corrections to the Kohn-Sham energy levels are included. The two physically motivated energy level corrections applied to improve the QP description by Quek and co-workers are illustrated in fig. 5 and result in a significantly improved theoretical prediction of the current in good agreement with the reported measurements. Firstly, it is well known that DFT will generally underestimate the fundamental gap of small organic molecules such as BDA. To account for this fact, Quek *et al.* considered an isolated BDA molecule by comparing the Kohn-Sham HOMO energy level to the experimental ionization energy (IP) [41]. The difference in energy between the experimental and Kohn-Sham IPs is then used to compensate for the unphysical electron self-interaction. The energy difference is determined to be roughly -3.0 eV and this value is also taken to estimate the correction required when the molecule is bonded between two metallic electrodes. The second correction term applied is to include the effects of the image charge potential as described in for example refs. [10, 11, 16]. This correction term is designed to adjust the Kohn-Sham energy levels to better estimate the fundamental energy gap of molecules near or adsorbed on a metal surface. The image potential accounts for the interaction between the molecular charge distribution in the vicinity of a metal surface. This effect is not accurately described within DFT calculations when using the GGA XC functional as well as for many other XC approximations. The image potential correction is estimated by calculating the energy due to an image charge induced on a perfectly conducting plane at a given distance from a point charge. For the case of the BDA MTJ, this effect is estimated to provide a +1.0 eV shift to the molecular HOMO in the junction. The overall effect is the energy level from the uncorrected Kohn-Sham calculation (molecular HOMO in this discussion) being lowered by approximately -2.0 eV relative to  $E_F$ . The resulting barrier height for hole transport is increased thereby resulting in reduction to the current magnitude and producing an approximation in close agreement with experiment.

Both of the correction terms as described can be cast in terms of electron removal or

FIG. 5: Corrections to the transport levels used in ref. [11]. The transport levels of the junction are adjusted with two terms: one to account for the underestimation of the IP difference between DFT with the GGA and experiment for an isolated molecule (left, 'DFT', and middle, 'Vacuum' respectively). The second term is what causes the fundamental gap to shrink when the molecule is adsorbed onto a conducting surface (blue arrows): the conductor screens any charge present on the molecule.

transfer processes, and to continue with the comparison between MECS and the corrected NEGF+DFT, it is necessary to consider how to define similar energies from the many-electron wavefunction treatment of the MTJ. Pickup and Gościński show that ionization potentials and electron affinities can be calculated perturbatively from a many-body wave function using the one-body Green's function [42]. Their analysis relies on Hartree-Fock orbitals in which the first order corrections vanish but which can be generalized for the use of Kohn-Sham orbitals and allows for a direct comparison to the QP picture. Here an alternative approach relating the CI energies and wavefunctions directly to the QP energies is used to define the potential barrier height.

To identify the molecular states in the junction that are hybridized with the electrode states, a procedure analogous to a Mulliken population analysis is performed. The total charge for a normalized molecular orbital is unity and can be calculated for the  $i^{\text{th}}$  MO  $\phi_i$  expanded in a basis of atomic orbitals  $\xi_j$  as

$$Q_i = e \langle \phi_i | \phi_i \rangle = e \sum_{j,k} c_{j;i}^* \langle \xi_j | \xi_k \rangle c_{k;i} = e, \quad (8)$$

where  $c_{j;i}$  is the coefficient of the  $j^{\text{th}}$  AO in the  $i^{\text{th}}$  MO, the summations over  $j, k$  extend over all AOs, and  $e$  is the electron charge in atomic units ( $e = 1$  a.u.). Restricting the summations to only AOs centered on the atoms comprising the BDA molecule, an estimate for the fraction of the charge in a junction orbital residing on the BDA molecule is obtained. Significant charge localized on the BDA molecule for an energy level in the vicinity of the transmission resonance seen below the Fermi level in fig. 2 are chosen as candidate states for the molecular HOMO in the junction. The charge contributions from AOs localized on the BDA molecule for several energetically higher lying occupied MOs are shown in fig. 6. The shaded area highlights the energy ranging approximately between  $E_F - 1.0$  eV and  $E_F - 0.5$

FIG. 6: Charge density on the molecule for several MOs at energies near the first transport resonance peak below  $E_F$ . The range covers sixteen MOs, but not all have charge contributions large enough to be visible on the plot. The two MOs with largest charge densities are retained as strongly hybridized molecular HOMOs.

eV, corresponding to the onset of the transport resonance in the NEGF+DFT calculations. Within this energy range, two MO levels display appreciable charge density in the molecular region indicating hybridization to the metal electrode states.

To determine the alignment of these molecular frontier states within the MTJ to the metal electrode work function after the introduction of electron correlations, the vertical IPs are calculated for the two molecular states with the highest charge densities in the energy range of interest. To determine the IP estimates requires two CI calculations to be performed, the first is for the neutral  $N$  electron model of the MTJ and the second is for a vertical ionization process from the molecular hybridized states for  $N - 1$  electron models of the MTJ. The ionization from the molecular level is approximated from the equilibrium or  $N$  electron ground state CI expansion by operating on it by the destruction operator  $a_i$  removing the  $i^{th}$  spin orbital

$$|\Psi^{N-1}\rangle = a_i|\Psi^N\rangle \quad (9)$$

to create a hole state. The CI energies are calculated for the  $N$  and  $N - 1$  many-electron states with the resulting IP estimate given as

$$\text{IP}_i = E_i^{N-1} - E^N, \quad (10)$$

where the subscript denotes the single electron state for which a hole has been introduced. The difference in energies between the ionization potential and the electrode work function then provides an estimate of the energy level alignment between the molecular hybridized states and the electrode work function. As before, the energy difference is then taken to approximate the potential barrier height in the junction. Thus by comparing the energy offsets predicted from the many-electron wavefunction calculations and the corrected QP treatments in relation to the the magnitude of the calculated MTJ conductances, the comparison between the two methods is achieved.

MO	lower	upper
IP (eV)	8.2	7.5
Barrier height (eV)	3.5	2.8

TABLE I: Approximate IPs and resulting MTJ potential barrier height obtained from CI calculations. Energy level offsets are determined relative to the estimated work function of Au electrodes of -4.7 eV.

Table I list the results from the CI estimates for the IP energies. As anticipated, electron correlations increase the IPs relative to DFT estimate using the GGA. At low voltage biases, the conductance will be dominated by the higher energy level which is taken to estimate the tunnel barrier for the MTJ. The electron correlation correction to the highest lying junction MO leads to a potential barrier height of 2.8 eV, and compares very well to the to the self-interaction and image potential corrected estimate for the barrier height of approximately 3.0 eV found by Quek *et al.* Both calculations when compared relative to the DFT/GGA of an approximately 1.1 eV barrier are expected to, and as demonstrated, produce significantly lower conductances than the NEGF+DFT estimate. Similar trends are seen in ref. [13] in which an explicit *GW* calculation for the gold-BDA-gold junction has been performed. From fig. 3 of ref. [13], the energy difference between the molecular HOMO and the gold Fermi energy is on the order of 2 eV, and the barrier height from their DFT calculation is on the order of 1 eV. Hence the *GW* calculation does not predict as large of an increase in the barrier height relative to the DFT estimate compared to this work and ref. [11]. However the results do agree in that a more accurate electronic structure description of the tunnel junction results in an increase barrier height leading to a reduction in the conductance. It should also be noted that the barrier heights obtained from the three methods used to account for the effects of electron correlation beyond approximate DFT produce conductance values that are within the range of experimental error. Hence the ability of the QP corrected transport levels and the MECS calculation to produce similar current magnitudes can be related to improved estimates of the potential barrier height in the simple tunnel model of a MTJ. Notably, it appears that a modest CI expansion can significantly improved the electronic structure description of the junction beyond a DFT/GGA calculation, and this description does not suffer from electron self-interaction errors due to its absence from the many-electron

Coulomb Hamiltonian used in the CI calculations. Additionally, the calculations suggest the CI treatment even with only moderate polarization can approximately correct for image charge effects.

#### IV. SUMMARY AND CONCLUSIONS

A comparison for the theoretical treatment of charge transport for the experimentally well characterized BDA MTJ has been undertaken. Two approaches are compared relative to NEGF+DFT calculations for the conductance of a BDA MTJ. Both approaches include corrections beyond a DFT/GGA description of the junction. In the work of Quek *et al.*, it was demonstrated that the net effect of treating Kohn-Sham energy levels as QP energies and providing self-interaction and image potential corrections can reproduce experimentally measured conductance values. In this study, an approach that explicitly includes correlations on the molecular junction through a many-electron wavefunction approach produces comparable results to the corrected K-S QP approach as well as the reported experimental measurements. The analysis reveals that a simple tunnel barrier model for the MTJ is treated comparably between two approaches for improving the electronic structure description beyond the reference NEGF+DFT calculation.

To perform the comparison, the MECS method was studied with respect to applying constraint conditions to the 1e-RDM obtained from the CI wavefunction for correlated electron transport. In particular, the sensitivity of the calculations to application of open system boundary conditions and limitations to current conservation were explored. Their effects based on reasonable physical considerations are found to be relatively moderate relative to experimental distributions for the BDA MTJ conductance. It should be noted that although the CI expansion used is defined with the use of Kohn-Sham orbitals, that the (non-relativistic) molecular Coulomb Hamiltonian defines the electronic structure for the MTJ for the MECS calculation. Effects from using approximations for the XC potential in DFT are absent, and hence improving a single determinant approximation by including a moderate level of electron correlation and polarizability can compare quite well to systematic corrections to the Kohn-Sham energy levels. Although conceptually and formally quite different, this work demonstrates that in the low voltage bias regime that a single particle picture of electron transport and a many-electron scattering approach

both provide predictions comparable to well defined experiments for the conductance of a MTJ consisting of a benzene diamine molecule bonded between two gold electrodes. The calculations reinforce the importance of predicting electronegativity in a MTJ to accurately treat charge transport [43]. In this regard, the ability to optimize ionization potentials and electron affinities in correlated orbital theories [44] suggests an attractive path forward if combined with NEGF methods to treat charge transport in molecular junctions.

## Acknowledgments

This work was funded in part by Science Foundation Ireland and additional support was provided by the Molecular Foundry funded by the Office of Science, Office of Basic Energy Sciences, of the U.S. Department of Energy under Contract No. DE-AC02-05CH11231. The authors are grateful to Professors Jeffrey Neaton and Zhenfei Liu for sharing details of their calculations. Recent support is provided by the Nottingham Ningbo New Materials Institute and the National Science Foundation of China with a project code 61974079.

## Data availability statement

The data that support the findings of this study are available from the Tyndall National Institute archives upon reasonable request.

- 
- [1] M. A. Reed, C. Zhou, C. J. Muller, T. P. Burgin, and J. M. Tour, *Science* **278**, 252 (1997)
  - [2] M. Di Ventura, S. Pantelides, and N. D. Lang, *Phys. Rev. Lett.* **84**, 979 (2000)
  - [3] G. Baym and L. P. Kadanoff, *Phys. Rev.* **124**, 287 (1961)
  - [4] L. V. Keldysh, *J. Exp. Theor. Phys.* **20**, 1018 (1965)
  - [5] R. Lake and S. Datta, *Phys. Rev. B* **45**, 6670 (1992)
  - [6] P. Hohenberg and W. Kohn, *Phys. Rev.* **136**, B864 (1965)
  - [7] K. Stokbro, J. Taylor, M. Brandbyge, and H. Guo, Ab-initio Non-Equilibrium Green's Function Formalism for Calculating Electron Transport in Molecular Devices. In: G. Cuniberti, K. Richter, G. Fagas (eds) *Introducing Molecular Electronics. Lecture Notes in Physics*, vol 680. Springer, Berlin, Heidelberg (2006)
  - [8] W. Kohn and L. J. Sham, *Phys. Rev.* **140**, A1133 (1965)
  - [9] R.W. Godby, M. Schlüter and L. J. Sham, *Phys. Rev. B* **37**, 10159 (1988)
  - [10] L. Kronik and Y. Morikawa, Understanding the Metal-Molecule Interface from First Principles. in: N. Koch, N. Ueno, and A. T. S. Wee (eds) *The Molecule-Metal Interface*, pp. 51-89, Wiley-VCH Weinheim (2013)
  - [11] S. Y. Quek, L. Venkataraman, H. J. Choi, S. G. Louie, M. S. Hybertsen, and J. B. Neaton,

Nano Lett. **7**, 3477 (2007)

- [12] P. Darancet, A. Ferretti, D. Mayou, and V. Olevano, Phys. Rev. B **75**, 075102 (2007)
- [13] M. Strange, C. Rostgaard, H. Häkkinen, and K. S. Thygesen, Phys. Rev. B **83**, 115108 (2011)
- [14] D. J. Mowbray, G. Jones, and K. S. Thygesen, J. Chem. Phys. **128**, 111103 (2008)
- [15] R. Stadler, V. Geskin, and J. Cornil, Phys. Rev. B **79** 113408 (2009)
- [16] J. A. Celis Gil and K. S. Thijssen, J. Chem. Phys. **147**, 084102 (2017)
- [17] P. Delaney and J. C. Greer, Phys. Rev. Lett. **93** 036805 (2004)
- [18] P. Delaney and J. C. Greer, Int. J. Quant. Chem. **100**, 1163 (2004)
- [19] J. C. Greer, Phys. Rev. B **83**, 245413 (2011)
- [20] M. Leijnse and M. R. Wegewijs, Phys. Rev. B **78** 235424 (2008)
- [21] A. E. Raeber and D. A. Mazziotti, Phys. Chem. Chem. Phys. **21** 12620 (2019)
- [22] M. Sajjan and D. A. Mazziotti, Commun. Chem. (Nature) **1**, 31 (2018)
- [23] A. E. Raeber and D. A. Mazziotti, arXiv preprint arXiv:2008.06028.
- [24] W. R. Frensley, Rev. Mod. Phys. **62**, 745 (1990)
- [25] G. Fagas, P. Delaney, and J. C. Greer, Phys. Rev. B **73**, 241314(R)(2006)
- [26] G. Fagas and J. C. Greer, Nanotechnology **18**, 424010 (2007)
- [27] S. McDermott, C. George, G. Fagas, J. C. Greer, and M. A. Ratner, J. Phys. Chem. C **113**, 744 (2009)
- [28] S. McDermott and J. C. Greer, J. Phys.: Condens. Matt. **24**, 125602 (2012)
- [29] R. Ahlrichs, M. Bär, M. Häser, H. Horn, and C. Kölmel, Chem. Phys. Lett. **162**, 165 (1989)
- [30] S. G. Balasubramani, G.P. Chen, S. Coriani, M. Diedenhofen, M. S. Frank, Y. J. Franzke, F. Furche, R. Grotjahn, M.E. Harding, C. Hättig, A. Hellweg, B. Helmich-Paris, C. Holzer, U. Huniar, M. Kaupp, A. Marefat Khah, S. Karbalaei Khani, T. Müller, F. Mack, B. D. Nguyen, S. M. Parker, E. Perlt, D. Rappoport, K. Reiter, S. Roy, M. Rückert, G. Schmitz, M. Sierka, E. Tapavicza, D. P. Tew, C. Wüllen, V. K. Voora, F. Weigend, A. Wodyński, and J. M. Yu, J. Chem. Phys **152**, 184107 (2020)
- [31] D. Sharma, L. Ansari, B. Feldman, M. Iakovidis, J. C. Greer, and G. Fagas, J. Appl. Phys. **113**, 203708 (2013)
- [32] J. C. Greer, J. Comp. Phys. **146**, 181 (1998)
- [33] L. Tong, M. Nolan, T. Cheng and J. C. Greer, Comp. Phys. Comm. **131**, 142 (2000)
- [34] J. P. Coe and M. J. Paterson, J. Chem. Phys. **138**, 209903 (2013)

- [35] J. C. Greer, *J. Chem. Phys.* **103**, 1821 (1995)
- [36] A. W. Prentice, J. P. Coe, and M. J. Paterson, *J. Chem. Phys.* **151**, 164112 (2019)
- [37] D. J. Thouless, *Nucl. Phys.* **21**, 225 (1960)
- [38] P. Carruthers and F. Zachariasen, *Rev. Mod. Phys.* **55**, 245 (1983)
- [39] M. Hillery, R. F. O'Connell, M. O. Scully, and E. P. Wigner, *Phys. Rep.* **106**, 121 (1984)
- [40] J. C. Greer, *Mol. Phys.* **106**, 1363 (2008)
- [41] Linstrom, P. J.; Mallard, W. G. NIST Chemistry WebBook; NIST Standard Reference Database Number 69; National Institute of Standards and Technology: Gaithersburg MD, 2005; [http:// webbook.nist.gov](http://webbook.nist.gov), 20899.
- [42] B. T. Pickup and O. Gościński, *Mol. Phys.* **26**, 1013 (1973)
- [43] I. Yeriskin, S. McDermott, R. J. Bartlett, G. Fagas and J.C. Greer, *J. Phys. Chem. C* **114**, 20564 (2010)
- [44] R. L. A. Haiduke and R. J. Bartlett **149**, 131101 (2018)

